Permeability computation of high resolution µCTscan with an unfitted boundary method to improve accuracy

Martin Lesueur[a,*], Hadrien Rattez[a] and Oriol Colomés[a]

[a] *Civil and Environmental Engineering, Duke University, Durham, NC 27708-0287, USA*

ARTICLE INFO

Keywords:
Flow simulations
Finite Element method
Permeability upscaling
µCT-scan
Unfitted boundary method

ABSTRACT

Flow simulations on porous media, reconstructed from Micro-Computerised Tomography (µCT)-scans, is becoming a common tool to compute the permeability of rocks. In order for the value of this homogenised hydraulic property to be representative of the rock at a continuum scale, the sample considered needs to be at least as large as the Representative Elementary Volume. Moreover, the numerical discretisation of the digital rock needs to be fine enough to reach numerical convergence. In the particular case of Finite Elements (FE), studies have shown that simulations should use structured meshes at least two times finer than the original image resolution in order to reach the mesh convergence. These two conditions and the increased resolution of µCT-scans to observe finer details of the microstructure, can lead to extremely computationally expensive numerical simulations. In order to reduce this cost, we couple a FE numerical model for Stokes flow in porous media with an unfitted boundary method, which allows to improve results precision for coarse meshes. Indeed, this method enables to obtain a definition of the pore-grain interface as precise as for a conformal mesh, without a computationally expensive and complex mesh generation for µCT-scans of rocks. From the benchmark of three different rock samples, we observe a clear improvement of the mesh convergence for the permeability value using the unfitted boundary method. An accurate permeability value is obtained for a mesh coarser than the initial image resolution. The method is then applied to a large sample of a high resolution µCT-scan to showcase its advantage.

1. Introduction

Micro-Computerised Tomography (µCT) was first developed to observe the microstructure of dense materials in a non-destructive way for applications such as medicine and material sciences (Tuan and Hutmacher, 2005; Salvo et al., 2003). It was later applied to rock materials and has shown to be a very valuable tool for rocks characterization (Mees et al., 2003; Cnudde and Boone, 2013). In particular, this technique is at the core of digital rock physics (Andrä et al., 2013; Arns et al., 2005). In this discipline, properties are measured and computed on µCT-scans of rocks such as: porosity (Arns et al., 2005; Blunt et al., 2013); mechanical properties (Arns et al., 2002); chemical properties (Godel, 2013); hydraulic properties (Arns et al., 2005; Blunt et al., 2013). We will focus on the latter in this contribution and compute the permeability based on flow simulations on µCT-scans images.

The concept of permeability was first introduced by Darcy (1856) as a quantification of the hydraulic conductivity of soils. This parameter plays a critical role in Darcy's law that is also used in rock mechanics to describe fluid flow at the reservoir scale. Permeability is therefore a key parameter to quantify for energy resources engineering (Bjorlykke, 2010). For this type of application, the property was previously measured using wireline-log analysis, well testing and core flooding experiments on samples collected from drilled wells (Ahmed et al., 1991). However, Darcy's law was proven to be a homogenisation of the Stokes formulation (Whitaker, 1986) for a Representative Element Volume (REV) of rock. The REV of any property is defined as the minimum sample size above which the value of the property assessed has converged to a steady-value. The investigation of the effect of the sample size on the results of simulations for Stokes flow simulations in µCT scans has been carried out for many different rock types (Mostaghimi et al., 2012). Since the REV of permeability for a rock is usually achieved at the scale of mm^3 (Guibert et al., 2015; Mostaghimi et al., 2012), at which µCT-scanning operates, more interest is building up on computing it directly on µCT-scans of the core sample, as being a faster and less expensive method than experimental measurements (Saxena et al., 2018). Indeed, the small sample size required for analysis makes it possible to produce multiple measurements on a single

*Corresponding author
martin.lesueur@duke.edu (M. Lesueur)
ORCID(s): 0000-0001-9535-2268 (M. Lesueur)

plug (Arns et al., 2005). Moreover, it enables the computation of hydraulic properties on core materials unsuitable to laboratory testing (Arns et al., 2004).

To compute the permeablity on CT-scan images, several approaches have been used to simulate the fluid flow including finite difference (Mostaghimi et al., 2012; Manwart et al., 2002) and finite element-based methods (Borujeni et al., 2013; Narváez et al., 2013), vortex and cell centred finite volume method (FVM) (Guibert et al., 2015; Petrasch et al., 2008) and lattice Boltzmann method (LBM) (Manwart et al., 2002; Narváez et al., 2013). The FVM and LBM are the most common approaches for this application (Song et al., 2019). However, the finite element method has gain interest recently as it allows to obtain permeabilities in a good agreement with LBM and FVM but at lower memory cost (Yang et al., 2019). Moreover, LBM and FVM are not the most suited methods when the fluid flow is coupled with other physical processes like mechanical deformation of the solid matrix. Such deformation can have a major effect on permeability evolution (Ghabezloo et al., 2009). In this context, Arbitrary Lagrangian-Eulerian approaches in finite elements are more commonly used (Lesueur et al., 2017). For these reasons, we are using the Finite Element method in this paper.

Resolution of CT-scans have been constantly improving since the technology was developed, obtaining now images above 1000^2 pixels and with a resolution below a few micrometres (Sarker and Siddiqui, 2009; Soulaine et al., 2016; Wang and Fleischmann, 2018). Higher resolutions for the CT-scans are particularly important for porous rocks in order to obtain a better characterization of the pore-grain interface like the detailing of grains' shape, which influences significantly the value of permeability obtained (Beard and Weyl, 1973; Cox and Budhu, 2008; Torskaya et al., 2013). Note that image processing methods also allow to improve on the quality of the microstructure recovered (Iassonov et al., 2009; Wang et al., 2019a). In this contribution, we focus on the CT-scan images after segmentation, thus we consider that the images present a well-defined pore-grain interface. The higher resolution mentioned comes with the constraint of a higher computational effort to run the flow simulation. Indeed, numerical accuracy is obtained when the result of the FE simulation converges towards a single value with decreasing size of the mesh elements, called mesh convergence. For permeability, the mesh convergence is only obtained with a mesh finer than the image resolution, which leads to simulations with a very large number of elements in the case of high resolutions CT-scans. For example, the study of Guibert et al. (2015) showed that a mesh size of even twice the resolution of the original image could not be enough to reach mesh convergence for permeability. In the case of carbonate rocks, it becomes then extremely difficult to get good accuracy on the value of permeability as the REV size can be very large (Mostaghimi et al., 2012; Liu et al., 2014). In some instances the size needed for the computation is above the capability of the simulator (Guibert et al., 2015) and final permeability value is only computed at the limit of resources.

While many solutions to the computational limit existing for high resolution CT-scans are developed with the objective to increase the number of elements in a simulation at a lower computational cost (Wang et al., 2019b), we opt for a different approach which aims at reducing the number of elements needed to reach mesh convergence. To this end, we are looking for a better approximation of the pore-grain interface for a mesh coarser than the CT-scan image resolution. Indeed, the magnitude of the approximation on permeability due to a too low resolution image is well documented in the literature (Guibert et al., 2015; Borujeni et al., 2013). Here we use an unfitted Finite Element Method (FEM) approach in which the geometry of the domain is embedded in a background mesh. Different methods can be considered here, typically classified in two main groups: immersed boundary methods or embedded boundary methods. The former basically consists on solving the problem in the active and inactive parts of the domain, enforcing the boundary condition via a forcing function (see Mittal and Iaccarino, 2005). In the later approach, the equations are solved only on the active part of the domain and the boundary conditions are enforced by either modifying the weak form of the problem or manipulating the mesh close to the boundary (see e.g. Burman et al., 2015; Rangarajan and Lew, 2014). In this work we propose an embedded boundary method for structured quadrilateral/hexahedral meshes in which the nodes of the background mesh at the interface between active and inactive elements are displaced in such a way that they fit the embedded geometry, see Section 2. Note that one of the main differences with respect to the universal meshes approach presented in (Rangarajan and Lew, 2014) is precisely the use of structured grids. By using structured grids we can take advantage of octree-based adaptive mesh refinement strategies (see e.g. Lesueur et al., 2017). Other advantages of this choice are, for instance, the ability to use spectral approximations or highly efficient data-structures.

After a first section on the description of this new method, referred as the displaced boundary method, it is benchmarked for μCT-scans of three types of rocks presenting different microstructure geometries. We finally showcase the method's performance for a high resolution CT-scanned rock sample.

2. Displaced boundary method description

The mesh of the digital rock is constructed using the approach introduced by Lesueur et al. (2017). It relies on the image reader capability of the finite element framework MOOSE (Permann et al., 2020) and produces 3D structured meshes of the pore space of rock microstructures reconstructed from a stack of segmented μCT-scan images. Our focus is when the image is so resolved that one needs to select a mesh coarser than the image resolution in order to restrain the computational burden to an acceptable level. In this case, the pore-grain boundary has to be grossly approximated in a given way. Specifically in this contribution, it is the pixel value of the element's centroid that dictates whether the element should be a pore or a grain. This meshing procedure is showcased for the example of a quarter circle in Fig. 1a and the resulting approximation of the boundary can be observed in Fig. 1b.

To use our method, we need to mesh the digital rock at its full resolution and extract the pore-grain boundary as a STL file. This file contains the geometry of the pore-grain interface that we are trying to match with the lower resolution mesh. As a preprocessing step, the distance between the exact interface given by the STL file and the approximated one of the mesh is computed. For each node of the meshed pore-grain boundary, we find the closest point on the STL and return the distance between the two. The distance is displayed for the example of a quarter circle in Fig. 1c. The nodes (and subsequently the integration points) of the mesh are then *displaced* of the computed distance and the pore-grain interface now matches the geometry of image at full resolution. The final result is a mesh with a lower resolution than the image that still matches closely the pore-grain boundary, as can be observed in the example of a quarter circle in Fig. 1d.

Note that this technique can be understood as a process to transform the original background mesh to a conforming mesh. However, it can also be understood as an unfitted FEM approach in which the mesh is fixed and an additional transformation map is applied to the Finite Element reference map. Indeed, this map ($\varphi_{\mathbf{d}}$) can be defined on all the mesh nodes as the identity for the interior nodes and the application of the distance field ($\mathbf{d}$) at the boundary (Γ), i.e. $\varphi : \mathbb{R}^d \to \mathbb{R}^d$ with

$$\hat{\mathbf{x}} = \varphi_{\mathbf{d}}(\mathbf{x}) = \begin{cases} \mathbf{x} + \mathbf{d} & \text{if } \mathbf{x} \in \Gamma, \\ \mathbf{x} & \text{otherwise.} \end{cases} \tag{1}$$

In this contribution, the "displaced mesh" refers to the equivalent mesh on which the FE simulations are computed.

The well-posedness of the method is guaranteed if the resulting map leads to transformed elements with a positive Jacobian. In that case, the method inherits all the convergence and stability properties of an standard conformal Finite Element approach. However, this condition is not satisfied in the general case. Nonetheless, in practice, the method of selecting the elements domain (pore or grain) based on the element's centroid (see Fig. 1a) results in an approximated pore-grain interface with a distance to the real interface of, at worst, one element's size h. Therefore, in practice, no negative jacobians should be found, which was observed in every simulation of this contribution. However further analysis is required to prove theoretical well-posedness. Another drawback of some unfitted FEM approaches is the so called *small cut-cell problem*, which results in ill-conditioned matrices caused by the appearance of active elements with a measure orders of magnitude smaller than the measure of the neighbouring elements. In the approach presented in this work this issue is avoided by only activating the elements whose centroid lies inside the domain. Therefore, assuming a sufficiently smooth boundary, the measure of the displaced elements is of the same order as the one of the elements from the original background mesh.

It is important to highlight that the proposed method does not depend on the way the geometry is characterized. That means that it can be used for geometries defined by STL files generated from CT-scanned samples, but also for domains defined by continuous distance fields, e.g the level-set method, or domains defined using CAD techniques. Furthermore, the proposed approach is suitable for non water-tied geometries, i.e geometries defined by non-contiguous parts, as long as a distance field can be provided at the pore-grain interface nodes.

Any computation during the simulation is done on the displaced mesh. The FEM simulator used in this contribution is MOOSE, in which we can do computations on the displaced mesh. The permeability computation is done following the methodology presented in Lesueur et al. (2017), summarised briefly below. Pressure driven stokes flow, expressed in dimensionless form as:

$$-\frac{1}{Re}\nabla^2 \vec{v_f}^{\,*} + \nabla p_f^* = 0 \tag{2}$$

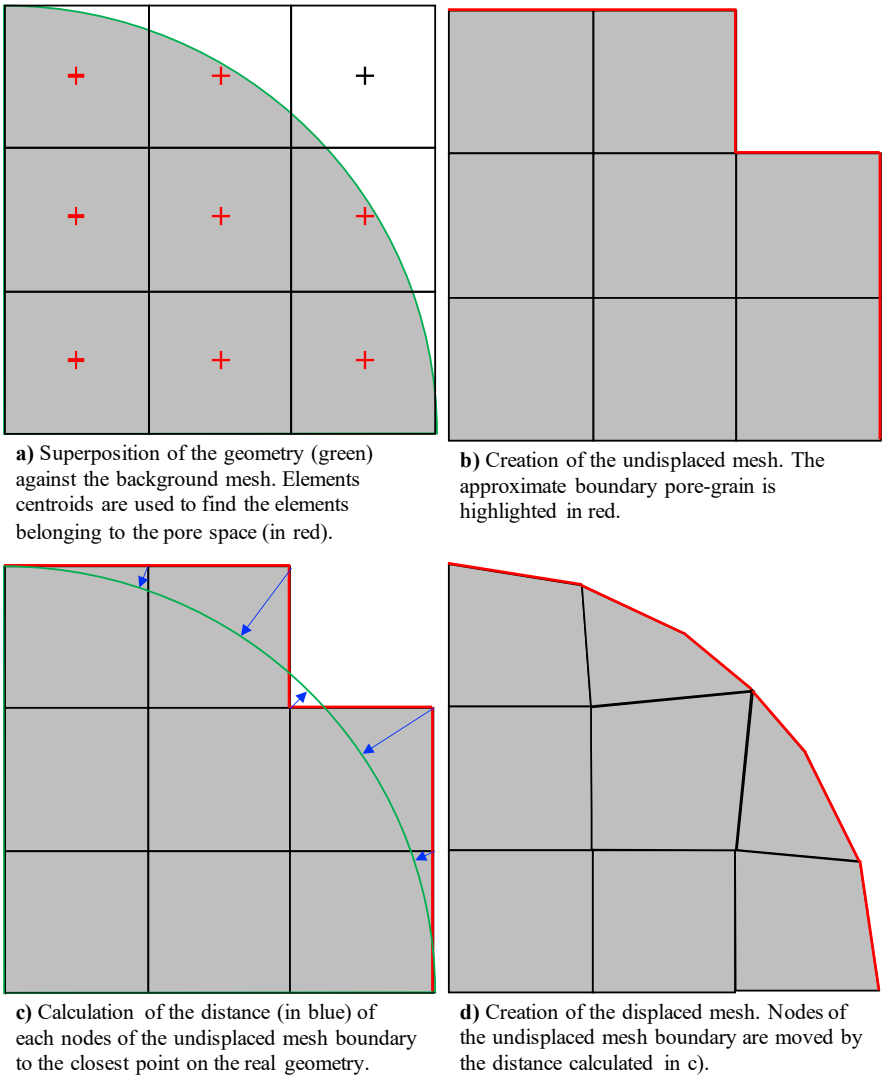

Figure 1: Schematic of the meshing procedure of a quarter circle against a 3x3 grid using the displaced boundary method. The displaced mesh (d) results in a better approximation of the real geometry than the undisplaced mesh (b).

$$-\nabla \cdot \vec{v_f}^* = 0 \tag{3}$$

is computed with MOOSE. Following Peterson et al. (2018) the system is stabilised with a Pressure-Stabilizing Petrov-Galerkin formulation, which allows to use simple first order elements instead of the classical Taylor-Hood elements to ensure the InfSup condition. Taking advantage of the solvers of PETSc included in MOOSE, the Schur method is used to precondition the system following Elman et al. (2008). We follow a prescribed solution from Balay et al. (2016) and use a Jacobi preconditioner for the fluid pressure subsystem and the algebraic multigrid method BoomerAMG (Henson and Yang, 2002) from HYPRE for the fluid velocity subsystem. Note that the preconditioning of our system enables to invert rigidity matrix even for elements for not well conditioned elements like in Fig. 1. From the computed flow, the average velocity in the selected direction is post processed on the displaced mesh. The permeability is finally calculated using the formula:

$$k = \mu_f \; L_{ref} \frac{\phi \; v_f^*}{\Delta p_f^*} \tag{4}$$

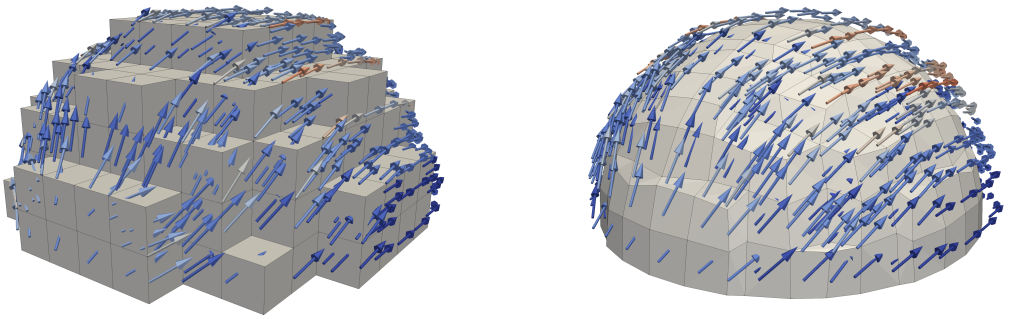

Figure 2: Oriented fluid flow vectors coloured with relative magnitude around a demi sphere, traditionally meshed (a) and displaced (b). The sphere is meshed with 10 elements in diameter for both figures.

The method is computationally very light, since the computation of the distances can be particularly efficient (we rely on the libigl library (Jacobson et al., 2018) in this contribution). In fact, for all the simulations presented in this study, using the displaced boundary method did not affect the computation time compared to the undisplaced mesh.

The influence of the method on the value of permeability is showcased conceptually in Fig. 2. A perfect semi sphere is meshed at a lower resolution in Fig. 2a, with 10 elements for the diameter. We use the displaced method to retrieve the smooth geometry of semi-sphere in Fig. 2b. The difference of geometry between the two meshes is reflected in the computed permeability through the porosity first, used in Eq. 4. In addition, this geometrical difference affects in turn the fluid flow. Instead of the fluid flowing through the virtual corners created by the boundary approximations in Fig. 2a, we observe the expected smooth flow around the displaced mesh of the sphere in Fig. 2b. This is the second influence on the permeability, specifically on the average velocity computed, which is used in the permeability formula, Eq. 4.

2.1. Poiseuille benchmark

We demonstrate the advantage of the method on a benchmark of the analytical solution for the permeability k of a 3D Poiseuille tube of radius R, $k = \pi R^4/8$. Poiseuille tubes were one of the first models of idealised porous media since their analytical permeability formula helps determining the permeability of the medium based on its porosity, a parameter easily measurable. We can imagine indeed the tubes to represent pore throats. For this reason, this section presents a suitable benchmark of the method for the computation of permeability on CT-scans.

The permeability is computed on both the approximately meshed tube and the displaced mesh. A mesh convergence is performed and we plot in Fig. 3 the error of the permeability compared to the analytical solution for both methods. We can see that the displaced method, in red, reaches below 1% of error very quickly, after only 20 elements in diameter, whereas the undisplaced mesh still is not under this value of 1% of error even at 150 elements in diameter. A similar magnitude of the error was observed by Yang et al. (2019). The reason why the permeability convergence of the undisplaced method is not smooth is that the volume on integration changes randomly for each mesh refinement step, as seen in the comparison of Fig 4 top and bottom left. We can also see in Fig. 3 the different orders of convergence between the undisplaced and displaced methods, linear and quadratic respectively. Note that in the undisplaced case, since we do not capture properly the boundary, the solution will be subject to an error at least of the order of the element size. Therefore, since we use stabilized linear Finite Elements with optimal quadratic convergence rate, see for instance Burman and Fernández (2011), the convergence rate of the solution will be at most linear. On the contrary, the proposed displaced approach results in a conformal discretization of the boundary, leading to the expected optimal convergence rate (quadratic). Such a smooth convergence allows to be more predictive on the extrapolation of the converged value.

3. Method performance

In order to showcase the method's performance on rock permeability computation, we compare the mesh convergence with and without the displaced boundary method for three completely different rock samples. We select the LV60A sandpack Imperial College Consortium On Pore-Scale Modelling (2014a), the S1 sandstone Imperial College

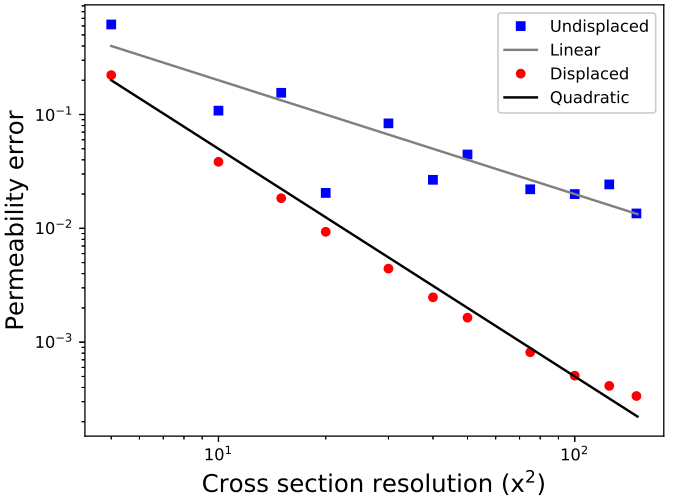

Figure 3: Permeability error compared to the analytical value for a tube of Poiseuille flow using both the undisplaced and displaced boundary method. Quadratic convergence of the error can be appreciated with the displaced boundary method (fitted with $5x^{-2}$ in black) while the undisplaced method has only a linear convergence (fitted with $2x^{-1}$ in grey).

Consortium On Pore-Scale Modelling (2014b) and finally, the Ketton limestone. As observed in Fig. 5, the nature of the rock studied changes its microstructure. In addition, the CT-scanning process influences the digitisation of said microstructure. The differences between the samples are listed below:

- **Granularity** The sandpack and the limestone are granular. It is harder to distinguish the grains in the sandstone as they are heavily cemented to each other. The rock matrix forms instead an interconnected skeleton.
- **Consolidation** A sandpack is known for being unconsolidated sand. We expect the sandstone to be more consolidated than the limestone as the porosity is a bit lower.
- **Texture** The sandpack grains are quite coarse; The sandstone has a fairly smooth interface; The limestone grains are extremely smooth.
- **Roundness** The sandpack and sandstone have grains that can be of various shapes, elongated or compact. The limestone instead have very round grains.
- **Grain size** The sandpack is known for having a very homogeneous grain size distribution. It differs from the limestone where a big contrast of size exists between some grains.
- **Resolution** The limestone has been CT-scanned at a much higher resolution than the other two rocks. We can almost visualise the pixels in Fig. 5a. The exact resolutions are listed in the caption of Fig. 5.

By selecting such a diverse array of samples, we aim at emphasising on the generic nature of the method, that can be applied to any rock's CT-scan.

The permeability is computed on 3D subsets of the samples of Fig. 5 using the flow simulator and permeability postprocessing of Sec. 2. For each sample, the mesh convergence of permeability is established with and without the displaced boundary method and the results are plotted in Fig. 6,7,8. We note that our method has no impact at the CT-scan original resolution because the distance computed would then be zero. However, a difference in resolution of one element is sufficient to fall back on the mesh convergence curve of the displaced method. The phenomenon is also present at half of the resolution of the CT-scan but is less impactful. In addition to the absolute value of permeability we also plot the error compared to the final value, computed respectively for each method. The two method are not evaluated against the same final value because our method converges to a different value than the undisplaced mesh, by a few %. This small difference can be explained by the fact that the displaced mesh is always smooth, i.e. not

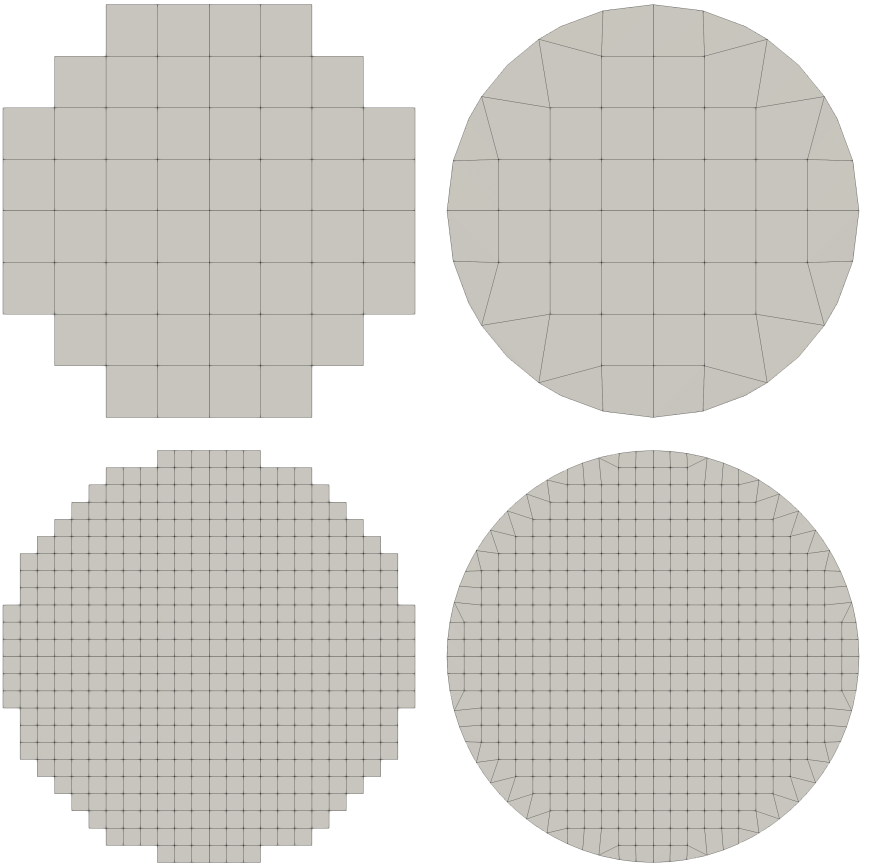

Figure 4: Visualisation of the mesh undisplaced (left) and displaced (right) for a higher resolution top to bottom.

pixelated, unlike the undisplaced mesh. This can be observed for example in Fig. 2,4. As shown in Fig. 3, this smoothness influences the results of permeability. Interestingly in the case of low resolution CT-scans, this difference could be considered an improvement considering that our method is able to retrieve the original smoothness of a rock, artificially pixelated during the CT-scanning process.

For all rock samples, we can observe that the mesh convergence is not reached at the image resolution with the undisplaced method, as confirmed by Guibert et al. (2015). We only manage to fall under 2% of error at twice the initial image resolution. Still, Guibert et al. (2015) showed that an even more accurate value can reached at four times the resolution of the initial image.

Using the displaced boundary method, we reach the mesh convergence (below 2% error) for each sample, always earlier than with the undisplaced method. Interestingly though, the convergence isn't reached for the same relative resolution. For the sandpack and the sandstone that have a similarly low resolution, respectively 10.002 µm and 8.683 µm, the convergence is achieved around the initial image resolution. However, it is for the limestone that has a high resolution of 3.00006 µm that our method performs the best. Mesh convergence is achieved at half of the image resolution.

By comparing the displaced boundary method with the undisplaced method, we expose that there exists actually two different convergences when running a mesh convergence of permeability.

The displaced boundary method exposes two different influences on the mesh convergence of permeability for regular meshing. The first one is the convergence of the geometry of the pore-grain boundary. Indeed with the undisplaced method, a matching geometry of the interface is only achieved at image resolution or one of its multiples. This could explain why Guibert et al. (2015) could not obtain a mesh convergence below the the image resolution, because the geometry would always be approximated under this resolution. The advantage of using our method is to be able to

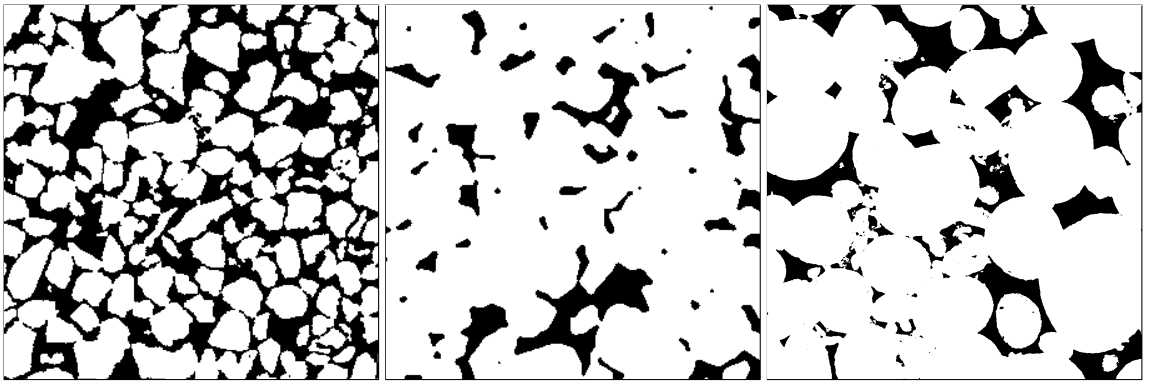

Figure 5: Visualisation of grains (white) and pore space (black) on a segmented slice of the samples studied. (a) The LV60A sandpack Imperial College Consortium On Pore-Scale Modelling (2014a) with a resolution of 10.002 µm (sample size of $(3\text{mm})^2$). (b) The S1 sandstone Imperial College Consortium On Pore-Scale Modelling (2014b) with a resolution of 8.683 µm (sample size of $(2.6\text{mm})^2$). (c) The Ketton limestone with a resolution of 3.00006 µm (sample size of $(3\text{mm})^2$).

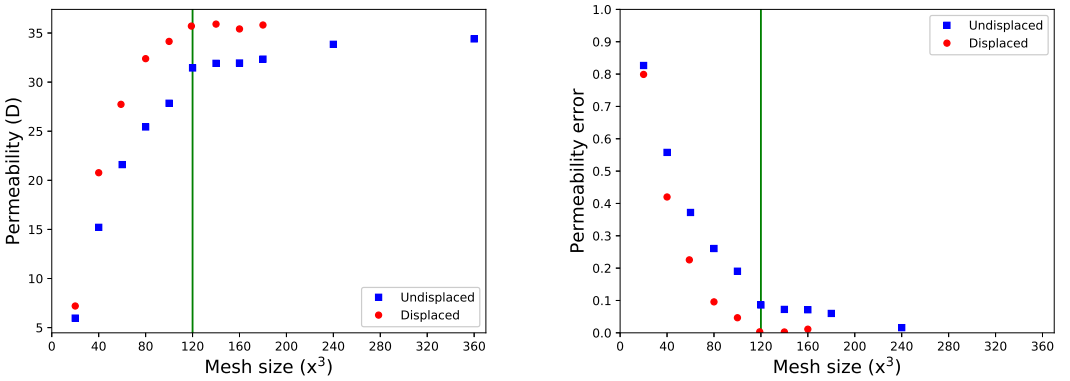

Figure 6: Mesh convergence of the permeability of a sample of the LV60A sandpack of size $(1.2\text{mm})^3$, with and without the displaced boundary method. The resolution of the original scan is 120^3 voxels. (a) shows absolute permeability computation and (b) the evolution of the permeability error compared to the final value.

have a good approximation of the interface very early. The second is the numerical mesh convergence itself. This one is achieved independently of the image resolution at a specific absolute value of mesh size h. High resolution images seems to be the most interesting application of our method because, in that case, the numerical mesh convergence is reached much earlier than the convergence of the geometry. Since our method is not affected by the convergence of the geometry, we therefore obtain a global mesh convergence much earlier than with the undisplaced method, as shown for the limestone sample in Fig. 8.

4. Application to high resolution CT-scan

After demonstrating the efficiency of the displaced boundary method for permeability computation on rocks' µCT-scan in the previous section, we apply it in the case where it is the most advantageous, for a high resolution CT-scan. We select again the Ketton carbonate on which our method has shown an impactful improvement on the cost of permeability computation (Fig. 8). However in this section, we select a larger sample, of 500^3 voxels in size, visualised in Fig. 10a. Since mesh convergence with the undisplaced method can only be reached at around two times the resolution of the original image, permeability should be computed on a sample of at least 1000^3 voxels. Since our system solves for the pressure and the velocity variables in each direction, this corresponds to solving for 4×10^9 Degrees Of Freedom (DOF). Running a flow simulation for such size requires obviously to be run on a supercomputer on which enormous

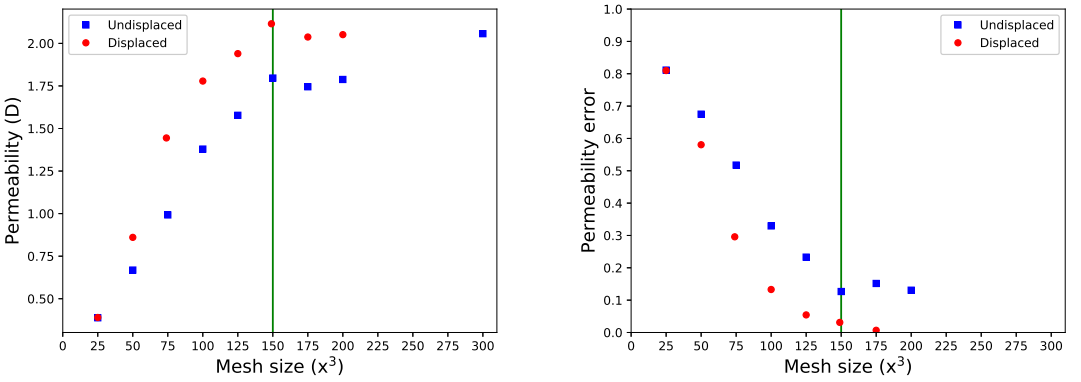

Figure 7: Mesh convergence of the permeability of a sample of the S1 sandstone of size $(1.3\text{mm})^3$, with and without the displaced boundary method. The resolution of the original scan is 150^3 voxels. (a) shows absolute permeability computation and (b) the evolution of the permeability error compared to the final value.

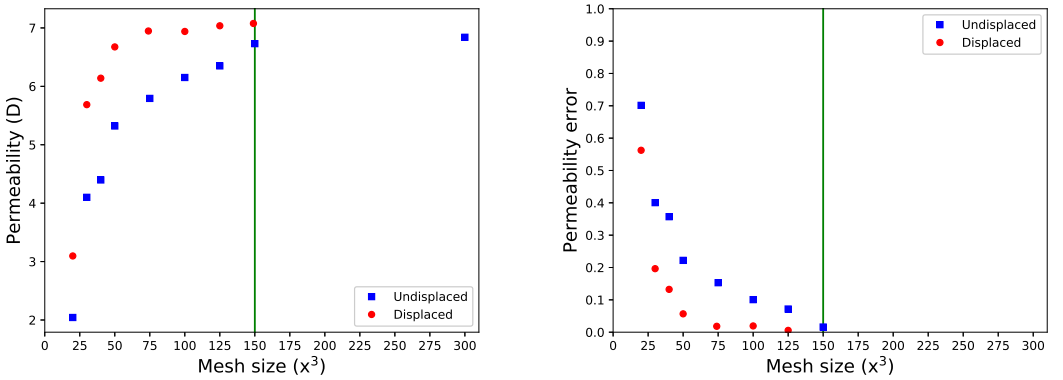

Figure 8: Mesh convergence of the permeability of a sample of the Ketton carbonate of size $(0.45\text{mm})^3$, with and without the displaced boundary method. The resolution of the original scan is 150^3 voxels. (a) shows absolute permeability computation and (b) the evolution of the permeability error compared to the final value.

memory allocation is needed. In our case, this size surpasses our solving capabilities. Yet we show in this section that the permeability of such a large sample can be retrieved easily with the displaced boundary method. In comparison, we also show how much error the undisplaced method still has at the limit of our resources.

The mesh convergence of the two methods is plotted in Fig. 9, in absolute values and with the relative error. Contrary to the previous benchmarking section, we simulate a real application of the method. Therefore the convergence is assessed at each increment of size by evaluating the relative error compared to the previous size selected, unlike the previous section where the absolute error is computed. Convergence is deemed reached under 2% error. It is achieved with the displaced boundary method at less than half the image resolution, similarly to Fig. 8. The improvement can be seen two ways. At the converged size of 200^3 voxels, it corresponds to a gain of 5% accuracy compared to the undisplaced method. On the other hand, if we expect the mesh convergence of this sample would normally be reached at 1000^3 voxels with the undisplaced method, using the displaced boundary method corresponds to saving $4 \times (1000 - 200)^3 \approx 2 \times 10^9$ DOF of computation, which is a consequent amount.

5. Conclusions

In this contribution, we have presented a method to improve the mesh convergence of permeability computations on µCT-scan. We have managed to do so by approximating the pore-grain geometry of the digital microstructure

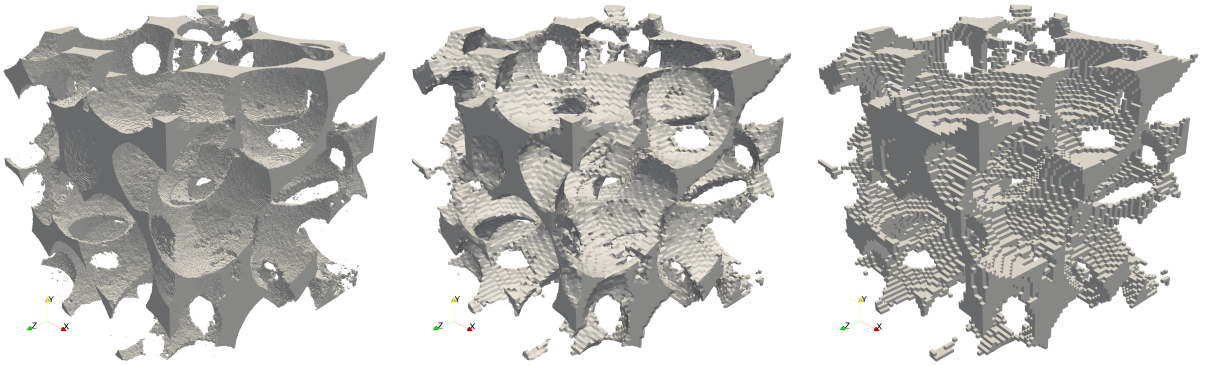

Figure 9: Visualisation of meshed pore space of the Ketton sample of size $(1.5\text{mm})^3$. (a) is the original scan composed of 500^3 voxels ; (b) is meshed with 75^3 elements with the boundary displaced to fit (a) ; (c) is meshed undisplaced with 75^3 elements.

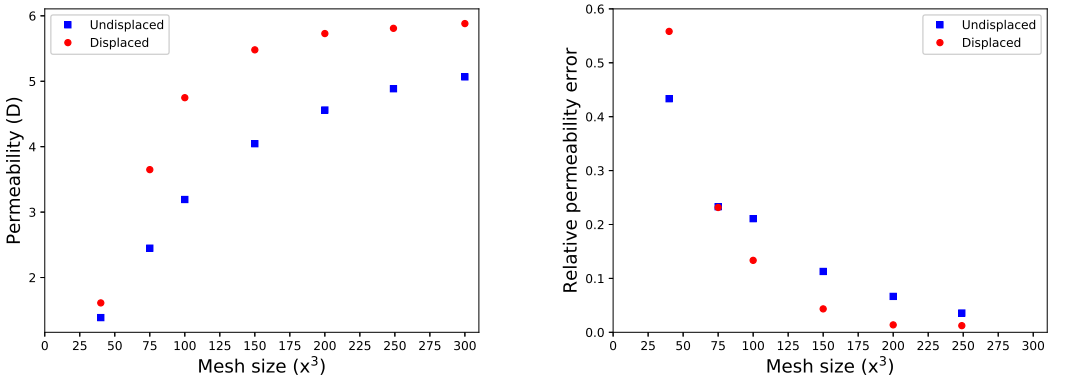

Figure 10: Mesh convergence of the permeability of a sample of the Ketton carbonate of size $(1.5\text{mm})^3$, with and without the displaced boundary method. The resolution of the original scan is 150^3 voxels. (a) shows absolute permeability computation and (b) the evolution of the permeability error compared to the consecutive value.

more accurately than regular meshing techniques. The unfitted boundary method used is implemented in the MOOSE simulation platform. The simulations are performed for an equivalent mesh, in which the nodes of the regular mesh close to the boundary are displaced to the closest point on the exact interface. The method has been benchmarked on the analytical solution of the Poiseuille tube (Sec. 2.1), shown to improve mesh convergence of permeability on three different digital rock samples of a sandpack, a sandstone and a limestone (Sec. 3) and finally applied to a high resolution CT-scan of a limestone (Sec. 4).

Our method allows to obtain a geometrical accuracy of the pore-grain boundary for very coarse meshes. In order to obtain global mesh convergence of the permeability, we only need to satisfy the absolute numerical mesh convergence. For this reason, our method is expected to perform better for high resolution CT-scans where the numerical mesh convergence is reached even for meshes coarser than the image resolution. Still, the unfitted boundary finite element method has been applied in this contribution to µCT images of digital rocks obtained after relatively coarse voxelised segmentation. However, the recent development of Super Resolution Convolutional Neural Networks (Wang et al., 2019a; Janssens et al., 2020) enable to produce high quality, high resolution images that are optimised for further segmentation and grey scale analysis of large samples. This unfitted boundary method would prove particularly useful by taking profit of the very high resolution pore-grain boundary resulting from more complex segmentation.

Finally, this method has only been applied here in the case of a static interface. However, multi-physical processes like mechanical deformations of the solid matrix (Lesueur et al., 2017) or dissolution-precipitation mechanisms (Lesueur et al., 2020; Rattez et al., 2019; Guevel et al., 2019) induce a displacement of the interface, which cannot

remain static during a simulation. The unfitted boundary method applied to flow coupled to these processes would allow to track accurately and in a continuous way the interface without at the same time requiring a very fine mesh.

References

Ahmed, U., Crary, S.F., Coates, G.R., 1991. Permeability estimation. The various sources and their interrelationships. Journal of Petroleum Technology 43, 578–587. doi:10.2118/19604-PA.

Andrä, H., Combaret, N., Dvorkin, J., Glatt, E., Han, J., Kabel, M., Keehm, Y., Krzikalla, F., Lee, M., Madonna, C., Marsh, M., Mukerji, T., Saenger, E.H., Sain, R., Saxena, N., Ricker, S., Wiegmann, A., Zhan, X., 2013. Digital rock physics benchmarks—part i: Imaging and segmentation. Computers & Geosciences 50, 25–32. doi:10.1016/j.cageo.2012.09.005.

Arns, C.H., Bauget, F., Limaye, A., Sakellariou, A., Senden, T., Sheppard, A., Sok, R.M., Pinczewski, V., Bakke, S., Berge, L.I., Oren, P.E., Knackstedt, M.A., 2005. Pore scale characterization of carbonates using x-ray microtomography. SPE Journal 10, 475–484. doi:10.2118/90368-pa.

Arns, C.H., Knackstedt, M.A., Pinczewski, W.V., Garboczi, E.J., 2002. Computation of linear elastic properties from microtomographic images: Methodology and agreement between theory and experiment. GEOPHYSICS 67, 1396–1405. doi:10.1190/1.1512785.

Arns, C.H., Knackstedt, M.A., Pinczewski, W.V., Martys, N.S., 2004. Virtual permeametry on microtomographic images. Journal of Petroleum Science and Engineering 45, 41–46.

Balay, S., Abhyankar, S., Adams, M.F., Brown, J., Brune, P., Buschelman, K., Dalcin, L., Eijkhout, V., Gropp, W.D., Kaushik, D., Knepley, M.G., McInnes, L.C., Rupp, K., Smith, B.F., Zampini, S., Zhang, H., 2016. PETSc Users Manual. Technical Report ANL-95/11 - Revision 3.7. Argonne National Laboratory.

Beard, D.C., Weyl, P.K., 1973. Influence of texture on porosity and permeability of unconsolidated sand. AAPG Bulletin 57. doi:10.1306/819a4272-16c5-11d7-8645000102c1865d.

Bjorlykke, K., 2010. Petroleum Geoscience: from Sedimentary Enviroments to Rock Physics. doi:10.1007/978-3-642-02332-3, arXiv:arXiv:1011.1669v3.

Blunt, M.J., Bijeljic, B., Dong, H., Gharbi, O., Iglauer, S., Mostaghimi, P., Paluszny, A., Pentland, C., 2013. Pore-scale imaging and modelling. Advances in Water Resources 51, 197–216. doi:10.1016/j.advwatres.2012.03.003.

Borujeni, A.T., Lane, N., Thompson, K., Tyagi, M., 2013. Effects of image resolution and numerical resolution on computed permeability of consolidated packing using LB and FEM pore-scale simulations. Computers & Fluids 88, 753–763. doi:10.1016/j.compfluid.2013.05.019.

Burman, E., Claus, S., Hansbo, P., Larson, M.G., Massing, A., 2015. Cutfem: discretizing geometry and partial differential equations. International Journal for Numerical Methods in Engineering 104, 472–501.

Burman, E., Fernández, M.A., 2011. Analysis of the pspg method for the transient stokes' problem. Computer methods in applied mechanics and engineering 200, 2882–2890.

Cnudde, V., Boone, M., 2013. High-resolution x-ray computed tomography in geosciences: A review of the current technology and applications. Earth-Science Reviews 123, 1–17. doi:10.1016/j.earscirev.2013.04.003.

Cox, M.R., Budhu, M., 2008. A practical approach to grain shape quantification. Engineering Geology 96, 1–16. doi:10.1016/j.enggeo.2007.05.005.

Darcy, H.P.G., 1856. Détermination des lois d'écoulement de l'eau à travers le sable, in: Les fontaines publiques de la ville de Dijon. V. Dalamont, pp. 590–594.

Elman, H., Howle, V.E., Shadid, J., Shuttleworth, R., Tuminaro, R., 2008. A taxonomy and comparison of parallel block multi-level preconditioners for the incompressible navier–stokes equations. J. Comput. Phys. 227, 1790–1808. doi:10.1016/j.jcp.2007.09.026.

Ghabezloo, S., Sulem, J., Saint-Marc, J., 2009. Evaluation of a permeability–porosity relationship in a low-permeability creeping material using a single transient test. International Journal of Rock Mechanics and Mining Sciences 46, 761–768. doi:10.1016/j.ijrmms.2008.10.003.

Godel, B., 2013. High-resolution x-ray computed tomography and its application to ore deposits: From data acquisition to quantitative three-dimensional measurements with case studies from ni-cu-PGE deposits. Economic Geology 108, 2005–2019. doi:10.2113/econgeo.108.8.2005.

Guevel, A., Rattez, H., Veveakis, M., 2019. Contact phase-field modeling for chemo-mechanical degradation processes. Part II: Numerical applications with focus on pressure solution. Preprint arXiv doi:arXiv:1907.00698.

Guibert, R., Nazarova, M., Horgue, P., Hamon, G., Creux, P., Debenest, G., 2015. Computational permeability determination from pore-scale imaging: Sample size, mesh and method sensitivities. Transport in Porous Media 107, 641–656. doi:10.1007/s11242-015-0458-0.

Henson, V.E., Yang, U.M., 2002. BoomerAMG: A parallel algebraic multigrid solver and preconditioner. Applied Numerical Mathematics 41, 155–177. doi:10.1016/s0168-9274(01)00115-5.

Iassonov, P., Gebrenegus, T., Tuller, M., 2009. Segmentation of x-ray computed tomography images of porous materials: A crucial step for characterization and quantitative analysis of pore structures. Water Resources Research 45. doi:10.1029/2009wr008087.

Imperial College Consortium On Pore-Scale Modelling, 2014a. Lv60a sandpack. doi:10.6084/m9.figshare.1153795.

Imperial College Consortium On Pore-Scale Modelling, 2014b. S1 sandstone. doi:10.6084/m9.figshare.1189274.v1.

Jacobson, A., Panozzo, D., et al., 2018. libigl: A simple C++ geometry processing library. Https://libigl.github.io/.

Janssens, N., Huysmans, M., Swennen, R., 2020. Computed tomography 3D super-resolution with generative adversarial neural networks: Implications on unsaturated and two-phase fluid flow. Materials 13. doi:10.3390/ma13061397.

Lesueur, M., Casadiego, M.C., Veveakis, M., Poulet, T., 2017. Modelling fluid-microstructure interaction on elasto-visco-plastic digital rocks. Geomechanics for Energy and the Environment 12, 1–13. doi:10.1016/j.gete.2017.08.001.

Lesueur, M., Poulet, T., Veveakis, M., 2020. Three-scale multiphysics finite element framework (FE3) modelling fault reactivation. Computer

Methods in Applied Mechanics and Engineering 365, 112988. URL: https://doi.org/10.1016/j.cma.2020.112988, doi:10.1016/j.cma.2020.112988.

Liu, J., Pereira, G.G., Regenauer-Lieb, K., 2014. From characterisation of pore-structures to simulations of pore-scale fluid flow and the upscaling of permeability using microtomography: A case study of heterogeneous carbonates. Journal of Geochemical Exploration 144, 84–96. doi:10.1016/j.gexplo.2014.01.021.

Manwart, C., Aaltosalmi, U., Koponen, A., Hilfer, R., Timonen, J., 2002. Lattice-boltzmann and finite-difference simulations for the permeability for three-dimensional porous media. Physical Review E 66. doi:10.1103/physreve.66.016702.

Mees, F., Swennen, R., Geet, M.V., Jacobs, P., 2003. Applications of x-ray computed tomography in the geosciences. Geological Society, London, Special Publications 215, 1–6. doi:10.1144/gsl.sp.2003.215.01.01.

Mittal, R., Iaccarino, G., 2005. Immersed boundary methods. Annu. Rev. Fluid Mech. 37, 239–261.

Mostaghimi, P., Blunt, M.J., Bijeljic, B., 2012. Computations of absolute permeability on micro-CT images. Mathematical Geosciences 45, 103–125. doi:10.1007/s11004-012-9431-4.

Narváez, A., Yazdchi, K., Luding, S., Harting, J., 2013. From creeping to inertial flow in porous media: a lattice boltzmann–finite element study. J. Stat. Mech: Theory Exp. 2013, 2–38. doi:10.1088/1742-5468/2013/02/p02038.

Permann, C.J., Gaston, D.R., Andrš, D., Carlsen, R.W., Kong, F., Lindsay, A.D., Miller, J.M., Peterson, J.W., Slaughter, A.E., Stogner, R.H., Martineau, R.C., 2020. MOOSE: Enabling massively parallel multiphysics simulation. SoftwareX 11, 100430. URL: http://www.sciencedirect.com/science/article/pii/S2352711019302973, doi:https://doi.org/10.1016/j.softx.2020.100430.

Peterson, J.W., Lindsay, A.D., Kong, F., 2018. Overview of the incompressible navier–stokes simulation capabilities in the MOOSE framework. Adv. Eng. Software 119, 68–92. doi:10.1016/j.advengsoft.2018.02.004.

Petrasch, J., Meier, F., Friess, H., Steinfeld, A., 2008. Tomography based determination of permeability, dupuit–forchheimer coefficient, and interfacial heat transfer coefficient in reticulate porous ceramics. Int. J. Heat Fluid Flow 29, 315–326. doi:10.1016/j.ijheatfluidflow.2007.09.001.

Rangarajan, R., Lew, A.J., 2014. Universal meshes: A method for triangulating planar curved domains immersed in nonconforming meshes. International Journal for Numerical Methods in Engineering 98, 236–264. doi:10.1002/nme.4624.

Rattez, H., Disidoro, F., Sulem, J., Veveakis, M., 2019. Influence of dissolution on the frictional properties of carbonate faults. Preprint EarthArXiv doi:10.31223/osf.io/b8xuh.

Salvo, L., Cloetens, P., Maire, E., Zabler, S., Blandin, J.J., Buffière, J.Y., Ludwig, W., Boller, E., Bellet, D., Josserond, C., 2003. X-ray micro-tomography an attractive characterisation technique in materials science. Nuclear Instruments and Methods in Physics Research, Section B: Beam Interactions with Materials and Atoms 200, 273–286. doi:10.1016/S0168-583X(02)01689-0.

Sarker, M., Siddiqui, S., 2009. Advances in micro-CT based evaluation of reservoir rocks, in: SPE Saudi Arabia Section Technical Symposium, Society of Petroleum Engineers. doi:10.2118/126039-ms.

Saxena, N., Hows, A., Hofmann, R., O. Alpak, F., Freeman, J., Hunter, S., Appel, M., 2018. Imaging and computational considerations for image computed permeability: Operating envelope of Digital Rock Physics. Advances in Water Resources 116, 127–144. URL: https://doi.org/10.1016/j.advwatres.2018.04.001, doi:10.1016/j.advwatres.2018.04.001.

Song, R., Wang, Y., Liu, J., Cui, M., Lei, Y., 2019. Comparative analysis on pore-scale permeability prediction on micro-CT images of rock using numerical and empirical approaches. Energy Science and Engineering 7, 2842–2854. doi:10.1002/ese3.465.

Soulaine, C., Gjetvaj, F., Garing, C., Roman, S., Russian, A., Gouze, P., Tchelepi, H.A., 2016. The impact of sub-resolution porosity of x-ray microtomography images on the permeability. Transport in Porous Media 113, 227–243. doi:10.1007/s11242-016-0690-2.

Torskaya, T., Shabro, V., Torres-Verdín, C., Salazar-Tio, R., Revil, A., 2013. Grain shape effects on permeability, formation factor, and capillary pressure from pore-scale modeling. Transp. Porous Media 102, 71–90. doi:10.1007/s11242-013-0262-7.

Tuan, H.S., Hutmacher, D.W., 2005. Application of micro CT and computation modeling in bone tissue engineering. Computer-Aided Design 37, 1151–1161. doi:10.1016/j.cad.2005.02.006.

Wang, J., Fleischmann, D., 2018. Improving spatial resolution at CT: Development, benefits, and pitfalls. Radiology 289, 261–262. doi:10.1148/radiol.2018181156.

Wang, Y.D., Armstrong, R.T., Mostaghimi, P., 2019a. Enhancing resolution of digital rock images with super resolution convolutional neural networks. Journal of Petroleum Science and Engineering 182, 106261. doi:10.1016/j.petrol.2019.106261.

Wang, Y.D., Chung, T., Armstrong, R.T., McClure, J.E., Mostaghimi, P., 2019b. Computations of permeability of large rock images by dual grid domain decomposition. Advances in Water Resources 126, 1–14. doi:10.1016/j.advwatres.2019.02.002.

Whitaker, S., 1986. Flow in porous media i: A theoretical derivation of darcy's law. Transp. Porous Media 1, 3–25. doi:10.1007/bf01036523.

Yang, L., Yang, J., Boek, E., Sakai, M., Pain, C., 2019. Image-based simulations of absolute permeability with massively parallel pseudo-compressible stabilised finite element solver. Computational Geosciences 23, 881–893. doi:10.1007/s10596-019-09837-4.